arXiv:1707.03074v3 [nlin.AO] 13 Dec 2019

Phenotypes of vascular flow networks

Henrik Ronellenfitsch[1, 2, *] and Eleni Katifori[2, †]

[1] *Department of Mathematics, Massachusetts Institute of Technology, Cambridge, MA 02139, USA*
[2] *Department of Physics and Astronomy, University of Pennsylvania, Philadelphia, PA 19104, USA*

(Dated: November 20, 2021)

Complex distribution networks are pervasive in biology. Examples include nutrient transport in the slime mold *Physarum polycephalum* as well as mammalian and plant venation. Adaptive rules are believed to guide development of these networks and lead to a reticulate, hierarchically nested topology that is both efficient and resilient against perturbations. However, as of yet no mechanism is known that can generate such networks on all scales. We show how hierarchically organized reticulation can be constructed and maintained through spatially correlated load fluctuations on a particular length scale. We demonstrate that the network topologies generated represent a trade-off between optimizing transport efficiency, construction cost, and damage robustness and identify the Pareto-efficient front that evolution is expected to favor and select for. We show that the typical fluctuation length scale controls the position of the networks on the Pareto front and thus on the spectrum of venation phenotypes.

Complex life would be inconceivable without biological fluid distribution networks such as animal vasculature, plant xylem and phloem, the network of fungal mycelia or the protoplasmic veins of *Physarum polycephalum*. These networks distribute oxygen and nutrients, remove waste and serve as long range communication pathways. In mammals, the vast spectrum of venation network phenotypes ranges from predominantly tree-like networks such as the large veins and arteries that service entire organs to highly reticulate capillaries within the organs such as in the brain or the liver. In plants, leaf network phenotypic variability even within a single organism can be large, but typically the hierarchical structure and reticulation are roughly conserved. However, within a single family there can be considerable variation [1]. It is therefore natural to ask whether there might be a single developmental mechanism at play that can generate and interpolate between the different archetypes on this phenotypic spectrum of vascular networks. Then, evolution would only need to select for a few parameters in order to tune the network phenotype for its function. Here, we theoretically identify fluctuations during development as such a mechanism, and pinpoint networks on a Pareto front possessing optimal trade-offs between hydraulic efficiency, damage resilience, and cost, as evolutionarily desirable.

Many frequently competing factors influence which particular phenotypes are favored by natural selection. Therefore, it is to be expected that the eventual physical form of an organism is shaped by trade-offs between different requirements. Pareto optimality identifies those phenotypes that strike optimal trade-offs between objectives: The Pareto front is the subset of phenotypes where performance at one objective can not be increased without decreasing performance at another {Fig. 1 (b), Ref. [2]}. One can assume that the phenotypes observed in nature are found approximately on some relevant Pareto front because any other trade-off could be improved upon and is therefore evolutionarily selected against, given otherwise fixed conditions [3].

In plants, where a well preserved fossil record of the venation exists, the fast transitions between reticulate and non-reticulate patterns over evolutionary time are evidence for an easily tunable mechanism generating vascular phenotypes [4, 5]. These transitions can also be effected artificially by single gene knockouts [6, 7] or small changes in phytohormone concentrations [8]. In the case of animals, often the positions and dimensions of the largest vessels (such as the aorta) are genetically predetermined and fixed. However, smaller vessels are too numerous to be efficiently genetically encoded and are believed to develop in a self-organized fashion [9–11]. The abstract mechanisms governing self-organization of vasculature in plants and animals appear to be universal [12]. For instance, in plant leaves, auxin canalization, involving flow of a chemical morphogen, is believed to guide development of the network pattern {Refs. [13–17], Fig. 1 (c,d)} and in animal vasculature, vessels respond to wall shear stress [10, 18–21]. Generically, these mechanisms involve a process that is able to remodel an initial mesh of veins according to the flow of blood (in animals), or cells connected by carrier proteins according to a morphogen (in plants). If the flow is large, vessels adapt by increasing their diameter; unused connections die out. This process has been observed directly in animals [22] and indirectly in plants [23].

Common to the vascular network development of both plants and animals, the dynamics of the hydraulic vessel conductivities K_e can be modeled by an equation of the form [12, 21, 24–26],

$$\frac{dK_e}{dt} = a\frac{(F_e^2)^\beta}{{K_e}^{\alpha-1}} - bK_e + c\,e^{-rt}, \tag{1}$$

where a, b, c and r are non-negative adaptation parameters and $\alpha \geq 1$, $\beta > 0$. Often, $\alpha = 1$ and $c = 0$. The dynamical steady states then correspond to different net-

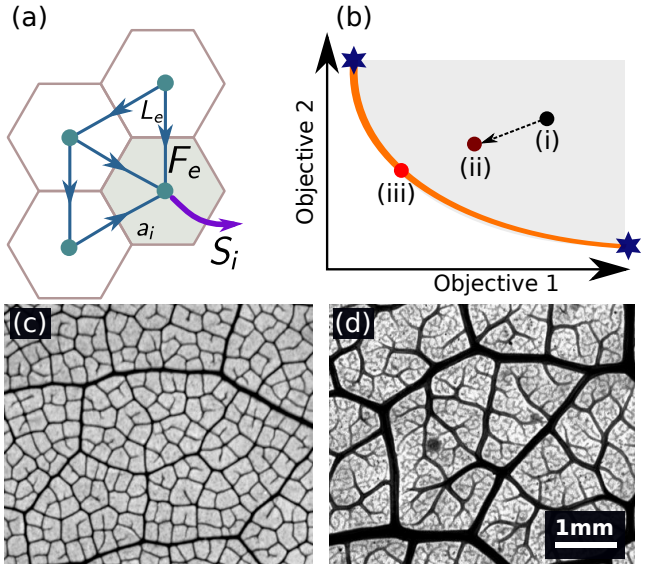


FIG. 1. (a) Network model of liquid transport. Edges e of length L_e carry currents F_e. At each node i, a net current S_i is drawn from the network. The net current S_i models local sources and sinks. (b) The Pareto front (orange) is the set of points out of all possible phenotypes (gray) for which performance can not be improved at both objectives simultaneously. For any point not on the Pareto front, e.g., (i), a different point can be found, e.g., (ii), that has better performance at both objectives. For a point on the Pareto front, like (iii), this is not possible. The endpoints of the Pareto front (stars) are functional archetypes. (c) Leaf veins of *Acer platanoides* near the "reticulate archetype" identified in this paper. (d) Leaf veins of *Protium dawsonii* show many freely ending veinlets, similar to what is found near the "tree archetype" identified in this paper.

work topologies.

Equation (1) describes a local positive feedback mechanism. Conductivities K_e grow as controlled by the magnitude of a when the current F_e through their vessel is large, and they decay on a characteristic time scale b^{-1} when it is small. The parameter c may be interpreted as the presence of some growth factor such as VEGF in the case of mammalian vasculature or background production of auxin transporting proteins in the case of plant leaves [25]. Potential flow is assumed throughout {Fig. 1 (a), Supplemental Material [27]}. An explicit time-dependence may exist during development, for instance due to growth of the surrounding tissue, or gradual depletion or degradation of the growth factor over a time scale r^{-1} [12].

The generic dynamics of Eq. (1) is characterized by two phases. First, the background production term dominates and produces a homogeneous network. Then, as background production becomes increasingly suppressed due to the exponential decay term, vascular adaptation takes over, generating veins in a hierarchical fashion: thick, main veins first and successively thinner veins later while pruning unused connections, comparable to vascular plexus development [18, 22, 28, 29]. The competition between background production and adaptation leads to hierarchically ordered steady-state networks [12], which are always topological trees [30, 31]. While non-hierarchical reticulation can be achieved by postulating new chemicals [32], we now introduce a model of adaptation to fluctuating load that can produce hierarchical reticulation. Such load fluctuations are common in animals (for instance Ref. [33]) and recent work points toward their existence in plants during development as well [23].

Assuming that the time scale on which fluctuations occur is much smaller than that of adaptation and that fluctuations are characterized by approximately static states between which the system switches quickly, we replace the squared currents in Eq. (1) by a fluctuation average [19, 24, 34–38],

$$F_e^2 \to \langle F_e^2 \rangle = \frac{1}{N} \sum_{\text{state } i} \left(F_e^{(i)} \right)^2 . \tag{2}$$

Here, the vector of fluctuating states $\mathbf{F}^{(i)} = (F_e^{(i)})$ represents the flows in the network for a particular vector of source terms $\mathbf{S}^{(i)} = (S_j^{(i)})$, and the summation performs an ensemble average for a given set of fluctuating states. Then, dynamical steady states can correspond to minima of optimization models [24, 34, 35].

We generalize these approaches to include collectively produced fluctuations by using the sources,

$$\frac{S_j^{(i)}}{\hat{S}} = \delta_{j0} - (1 - \delta_{j0})\, f\left(\frac{\|\mathbf{x}_j - \mathbf{x}_i\|}{\sigma} \right), \tag{3}$$

where $\mathbf{x}_i$ is the position of node i, σ is the scale over which the source strength varies, and $\sum_j S_j^{(i)} = 0$. The total in- and outflow is $\hat{S}$. In the rest of this paper we consider Gaussian sources ($f(x) \sim e^{-x^2/2}$). Other $f(x)$ lead to qualitatively similar results (Supplemental Material [27]). Uncorrelated fluctuations are obtained as $\sigma \to 0$ and lead to reticulation, but not to significant hierarchical ordering, similar to Fig. 2 (a,f).

We numerically solve a dimensionless form of Eq. (1),

$$\frac{d\tilde{K}_e}{d\tilde{t}} = \langle \tilde{F}_e^2 \rangle^{\beta} - \tilde{K}_e + \kappa\, e^{-\tilde{t}/\rho}, \tag{4}$$

where the tilde denotes dimensionless quantities (Supplemental Material [27]). Following Ref. [12] we set $\alpha = 1$, with other values leading to similar conclusions. The control parameters are the dimensionless background strength $\kappa = (c/a)\hat{S}^{-2\beta}$, the decay timescale $\rho = b/r$, and the fluctuation scale σ. We further fix the nonlinearity at $\beta = 2/3$, which leads to the same steady-state networks as shear-stress adaptation [24]. This value also corresponds to a total network volume constraint [12, 35].

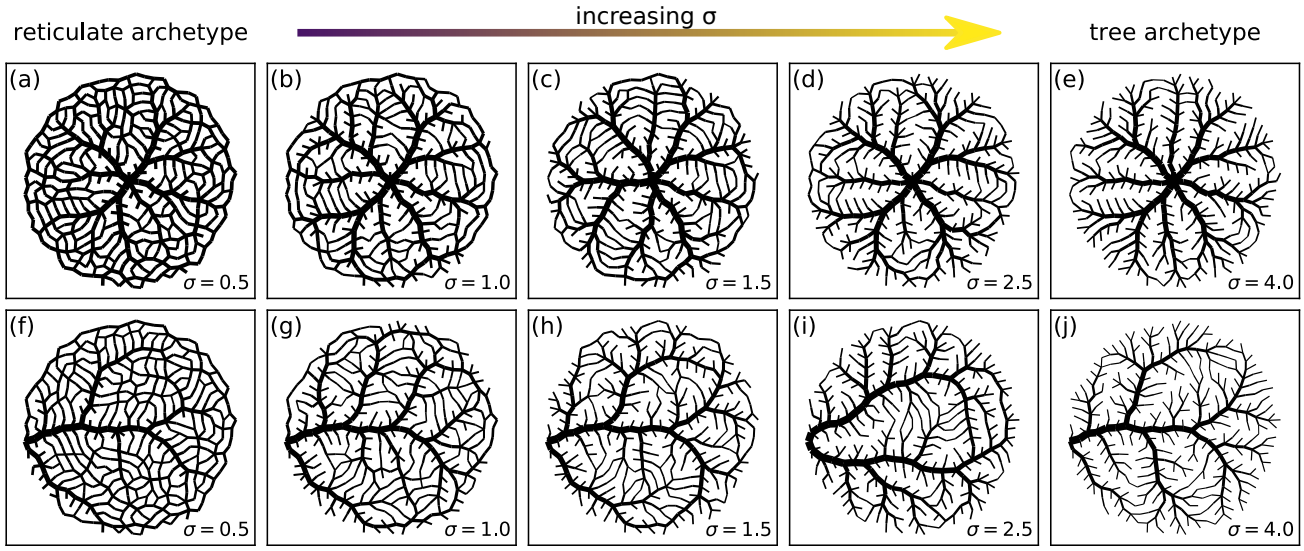


FIG. 2. The variety of network phenotypes that can be produced with a locally adaptive fluctuating load model. All examples lie on the Pareto front of efficient networks (Fig. 3), thus representing different trade-offs between baseline power dissipation, cost, and damage robustness. The number of loops and thus damage robustness increases to the right, the value of σ increases from 0.5 to 4.0 to the right. The Pareto front corresponds to the whole spectrum of "natural" reticulate networks, from highly hierarchical trees, fragile but cheap, to highly robust reticulate, expensive networks. (a)–(e) The inlet is at the center. (f)–(j) The inlet is at the left side.

All networks start from the same disordered mesh with 445 nodes and 1255 edges. We either place a single inlet at the center of the network, similar to the retina, or at the boundary, similar to a leaf. The conductivities are initialized with random positive numbers, and the scale parameter σ is measured in units of the mean edge length $\hat{L}$.

The interplay between background and decay parameters, fluctuation scale, and boundary conditions leads to a whole spectrum of networks, many of them qualitatively resembling the networks found in dicot and fern leaves, or the vasculature of the retina or the brain. They appear to reproduce well the hierarchical structure seen in real modern plants and animals (Fig. 2). Reticulation in particular is controlled by the fluctuation scale σ. For small $\sigma \ll \hat{L}$, the steady state networks are highly reticulate, similar to those obtained in Refs. [24, 35], and have little hierarchy [Fig. 2 (a),(b),(f),(g)]. As σ becomes comparable to or greater than $\hat{L}$, the networks gradually lose reticulation and gain hierarchical structure, independent of the chosen inlet position [Fig. 2 (c)–(e), (h)–(j)]. Intuitively, different large-scale sources $\mathbf{S}^{(i)}$ centered at nearby nodes overlap almost completely, and effectively act as a single state. Thus, the average is over only a few effective, large-scale sources, which leads to fewer effective fluctuations and therefore less reticulation. We develop a unified framework for arbitrary fluctuating sources by noting that the average flow can be rewritten as the weighted mean (Supplemental Material [27]),

$$\langle F_e^2 \rangle = \frac{1}{N} \sum_i \left(F_e^{(i)} \right)^2 = \sum_j \rho_j \left(R_e^{(j)} \right)^2 , \qquad (5)$$

where the ρ_j are the eigenvalues of the covariance matrix $\frac{1}{N} \sum_k \mathbf{S}^{(k)} (\mathbf{S}^{(k)})^\top$, and the $R_e^{(j)}$ are the flows induced by the associated eigenvectors as sources. For values of $\sigma \gg \hat{L}$, the collective sources themselves become highly correlated to each other, and the source covariance matrix is characterized by only a few dominant eigenvalues, with the vast majority negligibly small, independent of the specific form of $f(x)$ (Supplemental Material [27]). Armed with this model, we proceed to ask which of the network topologies it can produce may be favored by natural selection. We specialize to a single inlet at the center, with other inlet positions leading to qualitatively similar results (Supplemental Material [27]).

Hydraulic efficiency, low cost, and robustness are important but competing requirements, such that we expect that natural selection strikes a trade-off between them. As a measure of network efficiency, we consider the hydraulic power dissipation calculated under non-fluctuating conditions, $E = \sum_e L_e F_e^2 / K_e$, where the flows are computed for a single inlet and uniform sinks. The rationale is that during nominal operation, fluctuations are expected to be small, with large fluctuations to be expected during development. Next, the network cost, $C = \sum_e L_e K_e^\gamma$, where $\gamma < 1$ models an economy of scale, measures the amount of material investment that goes into constructing the network. This should be minimized

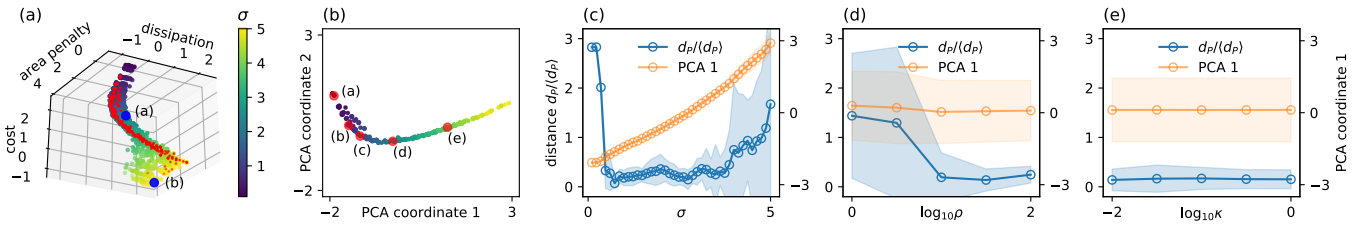


FIG. 3. Geometry of the Pareto front of adaptive distribution networks. We plot the phenotypic space of networks obtained from parameter values $\rho \in \{1, 10, 100\}$, $\kappa \in \{1, 0.1, 0.01\}$, $\sigma \in [0.1, 5]$, $\alpha = 1, \beta = 2/3$ as an example of the phenotypic space that can be reproduced using the model. We calculate the Pareto front for simultaneous minimization of power dissipation, network cost, and percolation penalty. The data was scaled to zero mean and unit variance in each objective. (a) The data set, colors indicate the value of σ. The Pareto front is in red, and the non-Pareto networks from Fig. 4 are in blue. (b) Principal component analysis (PCA) embedding of the Pareto front from (a). 91% of the variance is encoded in the first PCA coordinate, suggesting that the front is approximately one-dimensional. The first PCA coordinate (PCA 1) is approximately parametrizes the Pareto front. Red points correspond to the networks from Fig. 2 (a–e). (c) For all combinations (ρ, κ, σ) on the Pareto front P we hold ρ and κ fixed and vary σ. For a wide range of σ, the average distance $d_P(x) = \min_{p\in P} \|x - p\|$ from the Pareto front is well below the mean $\langle d_P\rangle$, suggesting that phenotypes remain close to the Pareto front (blue curve, shaded region is one standard deviation over combinations of ρ, κ). Varying σ moves linearly along the Pareto front parametrized by PCA 1 (orange curve). Thus, σ approximately parametrizes the Pareto front. Similarly varying ρ (d) or κ (e) while holding the other parameters fixed may lead to phenotypes close to the Pareto front for large ρ and all κ, but the position on the front PCA 1 is random. Thus, ρ and κ can not be used to parametrize the Pareto front.

by any organism that efficiently uses its resources. We set $\gamma = 1/2$, which corresponds to a cost proportional to the total vessel volume, or equivalently, total material used to construct the network. Finally, we consider a percolation penalty as a measure of network robustness, quantifying the cost of losing part of the vasculature to damage. We choose the expected fraction of perfused area lost upon removing an edge, $\hat{A} = (1/N_e)\sum_e A_e/A_{\text{tot}}$, where A_e is the area of the network that becomes disconnected from the source upon removal of edge e, A_{tot} is the total area of the network, and N_e is the number of edges. Efficient network phenotypes must minimize the cost C, the power dissipation E, and the percolation penalty A.

Observations of real networks, for instance in leaves, reveal that many treelike components exist and that they are important for transport [39]. This means that although the percolation penalty is minimized, it is not expected to be perfectly zero. Except for very small $\sigma \ll \hat{L}$ and very large $\sigma \gg \hat{L}$, network phenotypes obtained from our model generically exhibit these small treelike components within loops [Figs. 2, 4].

We scanned a portion of the parameter space and computed the three network measures for a data set of steady states of the adaptation dynamics. The steady state networks form a dense cloud in the space of network measures [Fig. 3 (a)]. Computing the Pareto front using the algorithm from Ref. [40] and analyzing its geometry using Principal Component Analysis (PCA) reveals an approximately one-dimensional line of points {Fig. 3 (b), Supplemental Material [27]}. Fixing ρ and κ, the parameter σ approximately parametrizes networks on the Pareto front [Fig. 3 (c–e)], such that σ can be used to tune optimal trade-offs between the three objectives. The endpoints of the Pareto front correspond to functional archetypes [3], on one end low-cost, fragile and non-reticulate, high dissipation networks ($\sigma \gg \hat{L}$, tree archetype), and on the other end high-cost, robust and fully reticulate, low dissipation networks ($\sigma \ll \hat{L}$, reticulate archetype) [Figs. 2, 3]. For small $\sigma \ll \hat{L}$, most networks lie close to the front, whereas for large $\sigma \gg \hat{L}$, there is greater variability, and many networks lie far from the front [Fig. 3 (a),(b)]. Defining a distance $d_P(x) = \min_{p\in P} \|x - p\|$ from the Pareto front P and rescaling all network measures to have unit variance and mean zero so as to bring them to the same scale, the mean distance from the front is $\langle d_P\rangle \approx 0.24$. The Pareto front comprises 14% of all networks. From the remaining ones, 70% lie closer than average to the front and 30% lie further than average from the front. Tuning κ by itself without fixing the other parameters has little

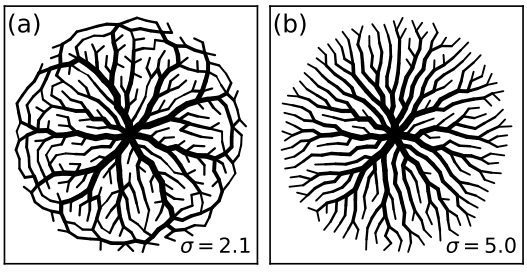


FIG. 4. Network phenotypes not lying on the Pareto front show less hierarchical organization for the same amount of reticulation than their Pareto optimal counterparts. In both networks, $\kappa = 1.0$, $\rho = 1.0$. (a) $E = 6.0$, $A = 0.48$, $C = 47.0$. (b) $E = 10.8$, $A = 7.73$, $C = 32.8$.

effect on the distance of networks from the Pareto front. However, $\rho \gtrsim 10$ or $0.5 \lesssim \sigma \lesssim 3$ can generically drive the network phenotypes close to the front (Supplemental Material [27]). Non-Pareto optimal phenotypes often show branching with parallel instead of roughly perpendicular veins (Fig. 4). Open, non-hierarchical venation patterns similar to those of some networks off the Pareto front can be found in in the leaves of the evolutionarily archaic *Ginkgo biloba* tree {Fig. 4 (b), Refs. [41, 42]}.

We have shown that a simple, easily tunable mechanism is able to produce an entire spectrum of phenotypic variation in vascular networks. The shape of networks on this spectrum can be rationalized by the interplay between flow fluctuations affecting developmental processes, and natural selection of parameters that lead to phenotypes on a Pareto front of optimal trade-offs between efficiency, cost, and resilience. The networks on the Pareto front are reminiscent of modern natural leaf or animal vasculature, suggesting that natural networks may be subject to the trade-offs we consider. Networks away from the Pareto front generically exhibit less hierarchical organization and less resemblance to modern plants and animals. Out of the three control parameters of our model, only the fluctuation scale is highly correlated to the position on the Pareto front and thus to the position on the spectrum of vascular networks. This could allow natural selection to more easily adjust for a given needed functionality, but also to re-use the same genetic pathway to construct networks with different functionality in the same organism. Beyond biology, engineered transport networks such as electrical power grids are often subject to similar trade-offs, such that we expect that our analysis will be useful here as well.

E.K. acknowledges support by NSF Award PHY-1554887, IOS-1856587, the University of Pennsylvania Materials Research Science and Engineering Center (MRSEC) through award DMR-1720530, the University of Pennsylvania CEMB through award CMMI-1548571, and the Simons Foundation through award 568888 and the Burroughs Welcome Career Award.

* henrikr@mit.edu
† katifori@sas.upenn.edu

[1] Henrik Ronellenfitsch, Jana Lasser, Douglas C. Daly, and Eleni Katifori, "Topological Phenotypes Constitute a New Dimension in the Phenotypic Space of Leaf Venation Networks," PLOS Computational Biology **11**, e1004680 (2015), arXiv:1507.04487.

[2] Kaisa Miettinen, *Nonlinear Multiobjective Optimization*, International Series in Operations Research & Management Science (Springer US, 1999).

[3] O. Shoval, H. Sheftel, G. Shinar, Y. Hart, O. Ramote, A. Mayo, E. Dekel, K. Kavanagh, and U. Alon, "Evolutionary Trade-Offs, Pareto Optimality, and the Geometry of Phenotype Space," Science **336**, 1157–1160 (2012), arXiv:9605103 [cs].

[4] T. J Givnish, J. C. Pires, S. W Graham, M. A McPherson, L. M Prince, T. B Patterson, H. S Rai, E. H Roalson, T. M Evans, W. J Hahn, K. C Millam, A. W Meerow, M. Molvray, P. J Kores, H. E O'Brien, J. C Hall, W. J. Kress, and K. J Sytsma, "Repeated evolution of net venation and fleshy fruits among monocots in shaded habitats confirms a priori predictions: evidence from an ndhF phylogeny," Proceedings of the Royal Society B: Biological Sciences **272**, 1481–1490 (2005).

[5] Benjamin Blonder, Bruce G. Baldwin, Brian J. Enquist, and Robert H. Robichaux, "Variation and macroevolution in leaf functional traits in the Hawaiian silversword alliance (Asteraceae)," Journal of Ecology **104**, 219–228 (2016).

[6] Quintin J Steynen and Elizabeth A Schultz, "The FORKED genes are essential for distal vein meeting in Arabidopsis." Development (Cambridge, England) **130**, 4695–4708 (2003).

[7] Francine Carland and Timothy Nelson, "CVP2- and CVL1-mediated phosphoinositide signaling as a regulator of the ARF GAP SFC/VAN3 in establishment of foliar vein patterns," Plant Journal **59**, 895–907 (2009).

[8] Thomas Berleth, Jim Mattsson, and Christian S. Hardtke, "Vascular continuity and auxin signals," Trends in Plant Science **5**, 387–393 (2000).

[9] F le Noble, V Fleury, A Pries, P Corvol, A Eichmann, and R S Reneman, "Control of arterial branching morphogenesis in embryogenesis: go with the flow." Cardiovascular research **65**, 619–28 (2005).

[10] Haymo Kurz, "Physiology of angiogenesis." Journal of Neuro-Oncology **50**, 17–35 (2001).

[11] Thi-Hanh Nguyen, Anne Eichmann, Ferdinand Le Noble, and Vincent Fleury, "Dynamics of vascular branching morphogenesis: The effect of blood and tissue flow," Physical Review E **73**, 061907 (2006).

[12] Henrik Ronellenfitsch and Eleni Katifori, "Global Optimization, Local Adaptation, and the Role of Growth in Distribution Networks," Physical Review Letters **117**, 138301 (2016).

[13] Richard S. Smith and Emmanuelle M. Bayer, "Auxin transport-feedback models of patterning in plants," Plant, Cell & Environment **32**, 1258–1271 (2009).

[14] Enrico Scarpella, "Control of leaf vascular patterning by polar auxin transport," Genes & Development **20**, 1015–1027 (2006).

[15] Carla Verna, Megan G. Sawchuk, Nguyen Manh Linh, and Enrico Scarpella, "Control of vein network topology by auxin transport," BMC Biology **13**, 94 (2015).

[16] Francois G. Feugier, A. Mochizuki, and Y. Iwasa, "Self-organization of the vascular system in plant leaves: Interdependent dynamics of auxin flux and carrier proteins," Journal of Theoretical Biology **236**, 366–375 (2005).

[17] Chrystel Feller, Etienne Farcot, and Christian Mazza, "Self-Organization of Plant Vascular Systems: Claims and Counter-Claims about the Flux-Based Auxin Transport Model." PloS one **10**, e0118238 (2015).

[18] Anne Eichmann, Li Yuan, Delphine Moyon, Ferdinand Lenoble, Luc Pardanaud, and Christiane Breant, "Vascular development: from precursor cells to branched arterial and venous networks," The International Journal of Developmental Biology **49**, 259–267 (2005).

[19] Dan Hu, David Cai, and Aaditya V Rangan, "Blood vessel adaptation with fluctuations in capillary flow dis-

tribution." PloS one **7**, e45444 (2012).
[20] M Scianna, C G Bell, and L Preziosi, "A review of mathematical models for the formation of vascular networks." Journal of theoretical biology **333**, 174–209 (2013).
[21] W J Hacking, E VanBavel, and J A E Spaan, "Shear stress is not sufficient to control growth of vascular networks: a model study," The American Journal of Physiology **270**, H364–75 (1996).
[22] Qi Chen, Luan Jiang, Chun Li, Dan Hu, Ji-wen Bu, David Cai, and Jiu-lin Du, "Haemodynamics-driven developmental pruning of brain vasculature in zebrafish." PLOS Biology **10**, e1001374 (2012).
[23] Danielle Marcos and Thomas Berleth, "Dynamic auxin transport patterns preceding vein formation revealed by live-imaging of Arabidopsis leaf primordia," Frontiers in Plant Science **5**, 235 (2014).
[24] Dan Hu and David Cai, "Adaptation and Optimization of Biological Transport Networks," Physical Review Letters **111**, 138701 (2013).
[25] Anne-Gaëlle Rolland-Lagan and Przemyslaw Prusinkiewicz, "Reviewing models of auxin canalization in the context of leaf vein pattern formation in Arabidopsis," The Plant Journal **44**, 854–865 (2005).
[26] Klaartje van Berkel, Rob J de Boer, Ben Scheres, and Kirsten ten Tusscher, "Polar auxin transport: models and mechanisms," Development **140**, 2253–2268 (2013).
[27] See Supplemental Material [url], which includes Refs. [43, 44].
[28] Vincent Fleury and Mathieu Unbekandt, "The Textural Aspects of Vessel Formation during Embryo Development and Their Relation to Gastrulation Movements," Organogenesis **3**, 49–56 (2007).
[29] Marcus Fruttiger, "Development of the retinal vasculature," Angiogenesis **10**, 77–88 (2007).
[30] Marc Bernot, Vincent Caselles, and Jean-Michel Morel, *Optimal Transportation Networks*, Lecture Notes in Mathematics, Vol. 1955 (Springer Berlin Heidelberg, Berlin, Heidelberg, 2009).
[31] Jayanth R Banavar, Francesca Colaiori, Alessandro Flammini, Amos Maritan, and Andrea Rinaldo, "Topology of the Fittest Transportation Network," Physical Review Letters **84**, 4745–4748 (2000).
[32] François G. Feugier and Yoh Iwasa, "How canalization can make loops: A new model of reticulated leaf vascular pattern formation," Journal of Theoretical Biology **243**, 235–244 (2006).
[33] Patrick J Drew, Andy Y Shih, and David Kleinfeld, "Fluctuating and sensory-induced vasodynamics in rodent cortex extend arteriole capacity." Proceedings of the National Academy of Sciences of the United States of America **108**, 8473–8478 (2011).
[34] Francis Corson, "Fluctuations and Redundancy in Optimal Transport Networks," Physical Review Letters **104**, 048703 (2010), arXiv:0905.4947.
[35] Eleni Katifori, Gergely J. Szöllősi, and Marcelo O. Magnasco, "Damage and Fluctuations Induce Loops in Optimal Transport Networks," Physical Review Letters **104**, 048704 (2010).
[36] Henrik Ronellenfitsch, Jörn Dunkel, and Michael Wilczek, "Optimal Noise-Canceling Networks," Physical Review Letters **121**, 208301 (2018), arXiv:1807.08376v2.
[37] Johannes Gräwer, Carl D. Modes, Marcelo O. Magnasco, and Eleni Katifori, "Structural self-assembly and avalanchelike dynamics in locally adaptive networks," Physical Review E **92**, 012801 (2015), arXiv:1405.7870.
[38] Erik Andreas Martens and Konstantin Klemm, "Transitions from trees to cycles in adaptive flow networks," Front. Phys. **5**, 1–10 (2017), arXiv:1711.00401.
[39] Lucia Fiorin, Timothy J Brodribb, and Tommaso Anfodillo, "Transport efficiency through uniformity: organization of veins and stomata in angiosperm leaves," New Phytologist **209**, 216–227 (2015).
[40] Marc Geilen and Twan Basten, "A Calculator for Pareto Points," in *2007 Design, Automation & Test in Europe Conference & Exhibition*, Vol. 2 (IEEE, 2007) pp. 1–6.
[41] Zhiyan Zhou and Shaolin Zheng, "The missing link in Ginkgo evolution," Nature **423**, 821–822 (2003).
[42] Veit Martin Dörken, "Morphology, anatomy and vasculature in leaves of Ginkgo biloba L. (Ginkgoaceae, Ginkgoales) under functional and evolutionary aspects," Feddes Repertorium **124**, 80–97 (2014).
[43] Joshua J. Blakeslee, Wendy A. Peer, and Angus S. Murphy, "Auxin transport," Current Opinion in Plant Biology **8**, 494–500 (2005).
[44] Eric M. Kramer and Malcolm J. Bennett, "Auxin transport: a field in flux," Trends in Plant Science **11**, 382–386 (2006).

Supplemental Material

Potential flow in vascular networks

Here, we describe a general framework capable of describing potential-driven flow of some quantity through a network that dynamically adapts its conductivities. Each node is taken to represent a unit of some subdivision of the underlying tissue, a basin that is fed by that node, with edges representing the flow between these basins either through vessels or via a facilitated diffusion process.

The current F_e through each edge e connecting adjacent units i and j is given by $F_e = K_e(p_j - p_i)/L_e$, where K_e is the dynamically adaptive conductivity, L_e is the length of the edge, and p_i is the potential (e.g., blood pressure or morphogen concentration) at unit i. In plants, proteins embedded in the plasma membrane are responsible for transporting auxin [43, 44] with facilitated diffusion constants K_e. In animals, blood flow through vessels can be approximated by Poiseuille's law $K_e = kR_e^4$ with a constant k and effective vessel radius R_e [19, 21].

Let $\Delta : \mathcal{N} \to \mathcal{E}$ be the network's oriented incidence matrix which maps the node vector space $\mathcal{N}$ to the edge vector space $\mathcal{E}$. The matrix Δ acts as a discrete difference operator. For each edge an arbitrary but fixed orientation is chosen (see Fig. 1 C in the main paper). Then the components $\Delta_{e,i}$ read:

$$\Delta_{e,i} = \begin{cases} 1, & \text{edge } e \text{ points towards node } i \\ -1, & \text{edge } e \text{ points away from node } i \\ 0, & \text{edge } e \text{ is not connected to node } i. \end{cases} \tag{S1}$$

The current vector $\mathbf{F} \in \mathcal{E}$ with entries F_e can be derived from the potentials $\mathbf{p} \in \mathcal{N}$ using the formula

$$\mathbf{F} = KL^{-1}\,\Delta\mathbf{p}, \tag{S2}$$

The conductivities and lengths are summarized in the diagonal matrices K and L.

The current balance at each node reads in vector form

$$\Delta^\top \mathbf{F} = \mathbf{S}, \tag{S3}$$

where $\mathbf{S}$ is the source (or net current) term. Eq. (S3) is Kirchhoff's current law. In plants, the source $\mathbf{S}$ describes the production rate of morphogen in each unit; in animals, it represents the amount of blood perfusing one area unit. Combining Eq. (S2) and Eq. (S3), we can solve for the steady state currents and obtain

$$\mathbf{F} = KL^{-1}\Delta(\Delta^\top KL^{-1}\Delta)^\dagger \mathbf{S}, \tag{S4}$$

where the dagger represents the Moore-Penrose pseudoinverse. Equation (S4) can be used to compute the currents given all other properties of the network.

Nondimensionalization of the model

Here, we explicitly derive the nondimensionalization of the dynamical equations presented in the main paper.

The dimensionful dynamical equations used in the main paper are

$$\mathbf{F} = KL^{-1}\Delta\left(\Delta^\top KL^{-1}\Delta\right)^\dagger \mathbf{S} \tag{S5}$$

$$\frac{dK_e}{dt} = a\left\langle F_e^2\right\rangle^\beta - bK_e + c\exp(-rt), \tag{S6}$$

where $\mathbf{F}$ is the flow state, a vector with elements F_e corresponding to the flows through each edge e. The source term $\mathbf{S}$ is the vector representing the net currents at each node. The parameters a, b, c determine the adaptive dynamics, r is an inverse time scale of decay of the background production term. K_e is he conductivity of edge e. The angle brackets denote an average over the contributions from all different fluctuating states. Finally, we assume that there is a typical scale $\hat{S}$ for the source strengths.

We choose the following nondimensionalization:

$$\begin{aligned} K &= \frac{a}{b}\hat{S}^{2\beta}\tilde{K}, \quad t = \frac{1}{b}\tilde{t}, \quad \mathbf{F} = \hat{S}\tilde{\mathbf{F}} \\ L &= \hat{L}\tilde{L}, \quad \mathbf{S} = \hat{S}\tilde{\mathbf{S}}. \end{aligned} \tag{S7}$$

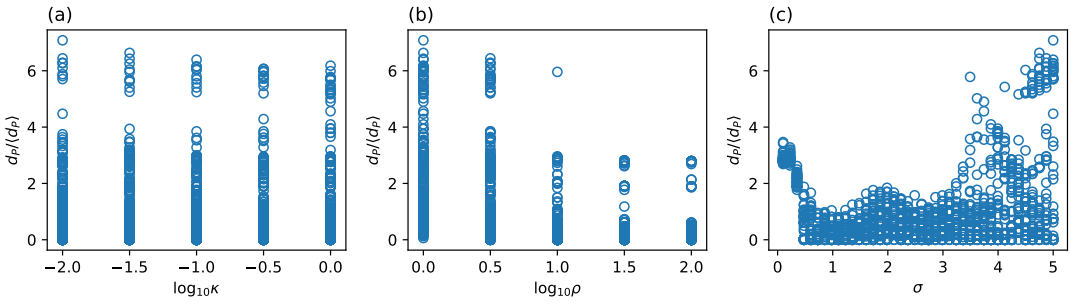


FIG. S1. Distance from the Pareto front $d_P(x) = \min_{p\in P} \|x - p\|$ for the scaled data set analyzed in the main paper. Distances are normalized by the average $\langle d_P\rangle$ over all points not on the Pareto front. We plot the distance as a function of the three simulation parameters. (a) Increasing the growth strength κ beyond $\kappa \approx 10$ can drive networks closer to the Pareto front. (b) The time scale ρ itself has little influence on distance from the Pareto front. (c) Fluctuation scales $0.5 \lesssim \sigma \lesssim 3$ lead to networks much closer to the Pareto front than other values.

The definitions of the symbols follow the main paper: K is the vessel conductivity, t is time, $\mathbf{F}$ is the current vector, L is the vessel length, and $\mathbf{S}$ is the source strength. Quantities with a tilde are dimensionless and quantities with a hat are typical scales. The model equations then reduce to the dimensionless system

$$\tilde{\mathbf{F}} = \tilde{K}\tilde{L}^{-1}\Delta\left(\Delta^\top \tilde{K}\tilde{L}^{-1}\Delta\right)^\dagger \tilde{\mathbf{S}} \tag{S8}$$

$$\frac{d\tilde{K}_e}{d\tilde{t}} = \langle \tilde{F}_e^2\rangle^\beta - \tilde{K}_e + \kappa\exp(-\tilde{t}/\rho), \tag{S9}$$

with the dimensionless control parameters $\kappa = (c/a)\hat{S}^{-2\beta}$, $\rho = b/r$.

Steady-state condition

We simulate the network dynamics until a steady state condition is reached. As a steady state measure, for each time step i we compute the dissipation

$$E_i = \sum_e \frac{\langle F_e^2\rangle}{K_e},$$

where the sum runs over all edges with $K_e > 10^{-8}$ (the nonzero edges). Then the simulation is ended once the relative change $|E_i - E_{i-1}|/|E_{i-1}| < 10^{-12}$, which we take as the condition that steady state has been reached.

Influence of the simulation parameters on distance from the Pareto front

In Fig. S1 we show the influence of the simulation parameters on the average distance from the Pareto front for the data set analyzed in the main paper. As a function of ρ, the distance is essentially random. As a function of κ, it is random for low values of κ, but networks are driven closer to the Pareto front for larger κ. As a function of σ, networks are close to the Pareto front for a range of medium values $0.5 \lesssim \sigma \lesssim 3$.

Algorithm for computing the Pareto front

Given a set of n observations of m objectives $Y = \{\mathbf{y}_n\}_n$ to be minimized, where $\mathbf{y} = (y_1, \ldots, y_m)$, we can introduce a partial ordering by defining $\mathbf{y} \prec \mathbf{y}'$ if $y_i \le y_i'$ for all i, and $y_j < y_j'$ for at least one j. We then say that $\mathbf{y}$ dominates $\mathbf{y}'$. The *Pareto front* is then the set

$$P = \{\mathbf{y} \in Y \mid D(\mathbf{y}) \text{ is empty}\}, \tag{S10}$$

Algorithm 1 Simple Cull algorithm for finding the Pareto front P, from Ref. [39].

```
P := {}
while Y ≠ {} do
    y := RemoveElementFrom(Y)
    dominated := False
    for each d ∈ P do
        if c ≺ d then
            P := P \ {d}
        else
            dominated := True, break.
        end if
    end for
    if not dominated then
        P := P ∪ {c}
    end if
end while
```

where the set

$$D(\mathbf{y}) = \{\mathbf{y}' \in Y \mid \mathbf{y}' \neq \mathbf{y} \text{ and } \mathbf{y}' \prec \mathbf{y}\} \tag{S11}$$

is the set of all points that dominate $\mathbf{y}$. Thus, the Pareto front is the set of all points that are not dominated by any other points. In order to find the Pareto front, we follow Ref. [39] from the main paper and implement their Algorithm 2 (Simple Cull). For reference, we reproduce pseudocode in Algorithm 1.

Principal Component Analysis

Given an $n \times m$ matrix of data $\mathbf{Y}$ with n observations of m objectives, where each column has mean 0 and variance 1, Principal Component Analysis computes the eigen-decomposition of $\mathbf{Y}^\top\mathbf{Y}$ (proportional to the covariance matrix of the data). The eigenvalues are then ordered from largest to smallest, and are proportional to the fraction of the total variance encoded in the component of the data in the direction of the corresponding eigenvector. If $\mathbf{v}_i$ is the i'th PCA eigenvector, then the corresponding i'th PCA coordinate (PCA i) of a point $\mathbf{y}$ (one row of $\mathbf{Y}$) is the inner product $\mathbf{v}_i^\top\mathbf{y}$.

In the main paper, the data matrix $\mathbf{Y}$ consists of the points on the Pareto front found using Algorithm 1. The PCA coordinates are then still well-defined for *any* point (not just Pareto points) and are computed using $\mathbf{v}_i^\top\mathbf{y}$.

Results for other boundary conditions and lattices

In this section we show computational results for other lattices, boundary conditions, and fluctuation functions. In all cases, we use the same parameter values as in the main paper.

The collectively produced fluctuations of the sources are generated by a function of the form:

$$\frac{\mathbf{S}_j^{(i)}}{\hat{S}} = \delta_{j0} - (1-\delta_{j0})\, f\left(\frac{\|\mathbf{x}_j - \mathbf{x}_i\|}{\sigma}\right), \tag{S12}$$

where $\mathbf{x}_i$ is the position of node i, σ is the scale over which the source strength varies, and $\sum_j \mathbf{S}_j^{(i)} = 0$. The function $f(x)$ determines the type of fluctuations. The total in- and outflow is $\hat{S}$.

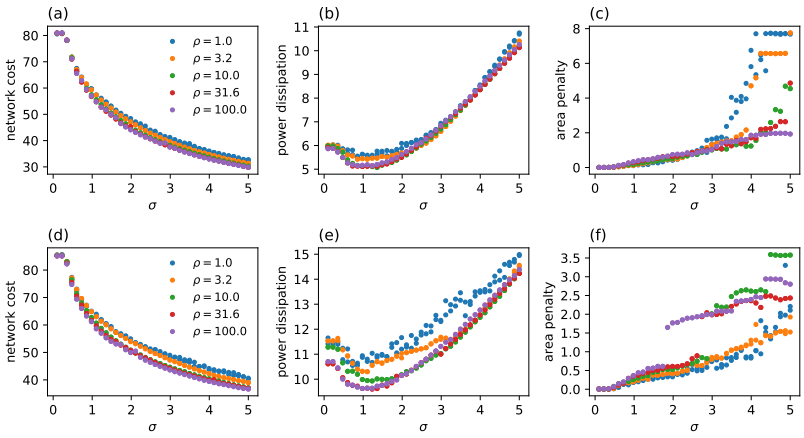


FIG. S2. Network measures for Gaussian sources at fixed $\kappa = 1.0$. (a–c) A single inlet at the center of the network. (d–f) A single inlet at the left side of the network.

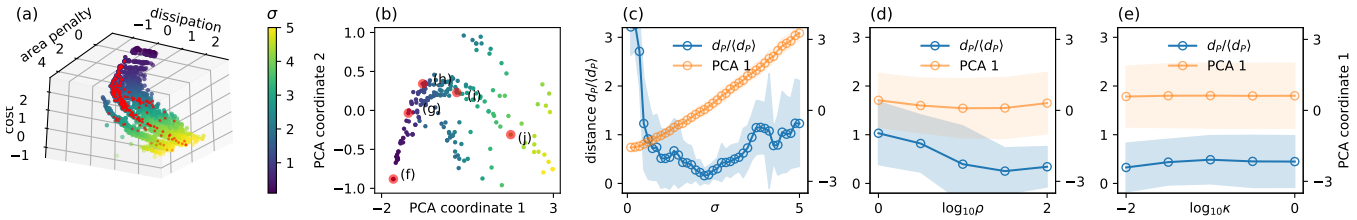


FIG. S3. Equivalent of Fig. 3 from the main paper for the case of Gaussian sources with an inlet at the left boundary of the network. The Pareto front shows distinctive branches which individually resemble one-dimensional curves. The other results are qualitatively similar to those for a centered inlet from the main paper. The marked networks in panel (b) correspond to the networks (f–j) from Fig. 2 in the main paper.

Gaussian sources

Here, we show results for Gaussian collective sources where the inlet is located at the left side of the network, in addition to the case considered in the main paper Gaussian sources are given by

$$f(x) \sim e^{-\frac{x^2}{2}}, \tag{S13}$$

where the constant of proportionality is computed from the condition $\sum_j S_j^{(i)} = 0$.

The network phenotypes show the same qualitative behavior as for the case of the main paper, where the source was at the center. The one exception is the percolation penalty (Fig. S2 (f)), which shows two branches. This is because as σ increases and the number of loops decreases, it becomes more likely that the source is only connected by a single edge to the rest of the network. In contrast, with the source in the center, this is unlikely to happen. This branching can also be seen in the phenotypic space and in the corresponding Pareto front (Fig. S3). Otherwise, the case of a single inlet at the left qualitatively agrees with the one from the main paper.

Furthermore, we investigated different values of the nonlinearity parameter β in the biologically relevant regime $\beta > 1/2$ (Smaller β lead to fully reticulate networks in all cases). Specifically, we looked that the case of center inlets. The results for $\beta = 0.77$ are shown in Fig. S4, and the results for $\beta = 0.63$ are shown in Fig. S5. Qualitatively, we obtain the same results as for $\beta = 2/3$, the case considered in the main paper.

In all cases (main paper and supplement), we scanned a parameter range of 5 logarithmically distributed points between $\rho = 1$ and $\rho = 100$, 5 logarithmically distributed points between $\kappa = 0.01$ and $\kappa = 1$, and 40 linearly distributed points between $\sigma = 0.1$ and $\sigma = 1$. For each combination, we took 2 samples with random initial conditions.

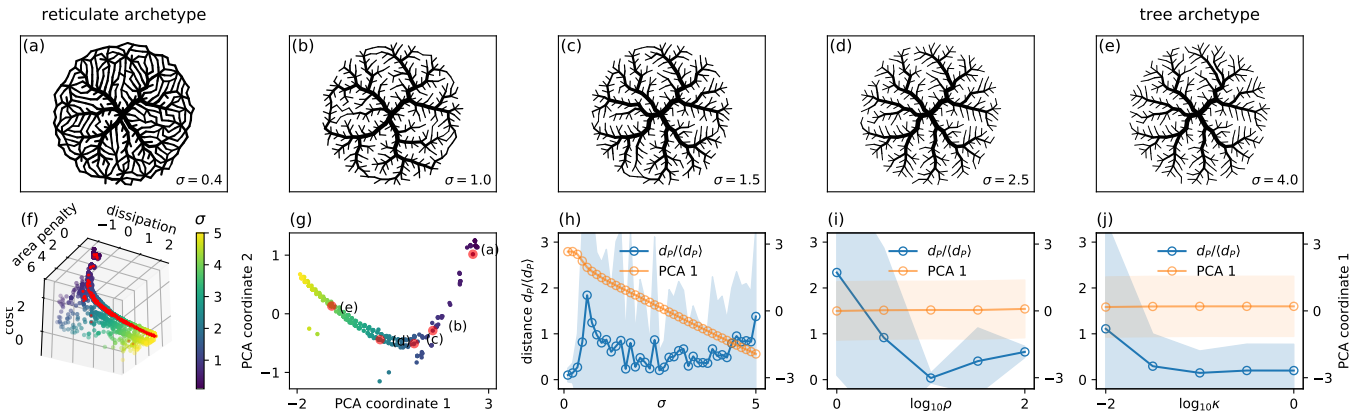


FIG. S4. Results for $\beta = 0.77$ with Gaussian sources and an inlet at the center of the network. (a–e) Network phenotypes along the Pareto front. (f) Task space with Pareto front in red. (g) PCA embedding of the Pareto front shows approximately 1-dimensional curve Labels (a–e) correspond to the networks shown in corresponding panels. (h–j) Equivalents to Fig. 3 (d–f) in the main paper show that σ parametrizes the Pareto front while κ and ρ do not.

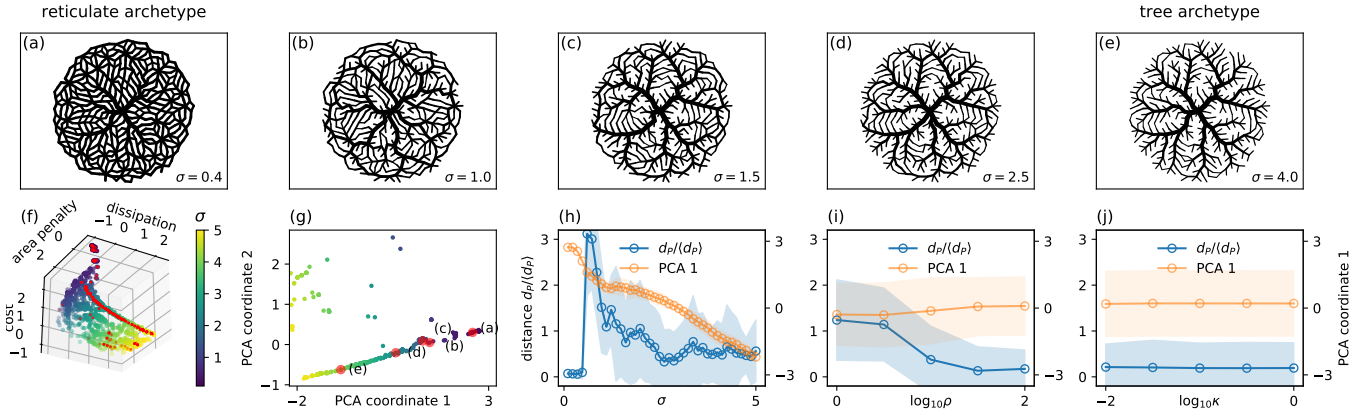


FIG. S5. Results for $\beta = 0.63$ with Gaussian sources and an inlet at the center of the network. (a–e) Network phenotypes along the Pareto front. (f) Task space with Pareto front in red. (g) PCA embedding of the Pareto front shows approximately 1-dimensional curve Labels (a–e) correspond to the networks shown in corresponding panels. (h–j) Equivalents to Fig. 3 (d–f) in the main paper show that σ parametrizes the Pareto front while κ and ρ do not.

Exponential sources

In this subsection we show results for exponential collective sources,

$$f(x) \sim e^{-x}. \tag{S14}$$

We find no qualitative difference between exponential and Gaussian distributed sources in the phenotypes as a function of σ or the phenotypic space. Fig. S6 shows the equivalent of Fig. 2 from the main paper for exponential sources.

Figs. S7 and S8 correspond to Fig. 3 from the main paper for inlets at the center and on the boundary of the network, respectively. Again we find qualitatively similar results to the case investigated in the main paper. For completeness, we show the dependence of the network measures on correlation length at fixed κ in Fig. S9.

In all cases, we scanned a parameter range of 5 logarithmically distributed points between $\rho = 1$ and $\rho = 100$, 5 logarithmically distributed points between $\kappa = 0.01$ and $\kappa = 1$, and 40 linearly distributed points between $\sigma = 0.1$ and $\sigma = 1$. For each combination, we took 2 samples with random initial conditions.

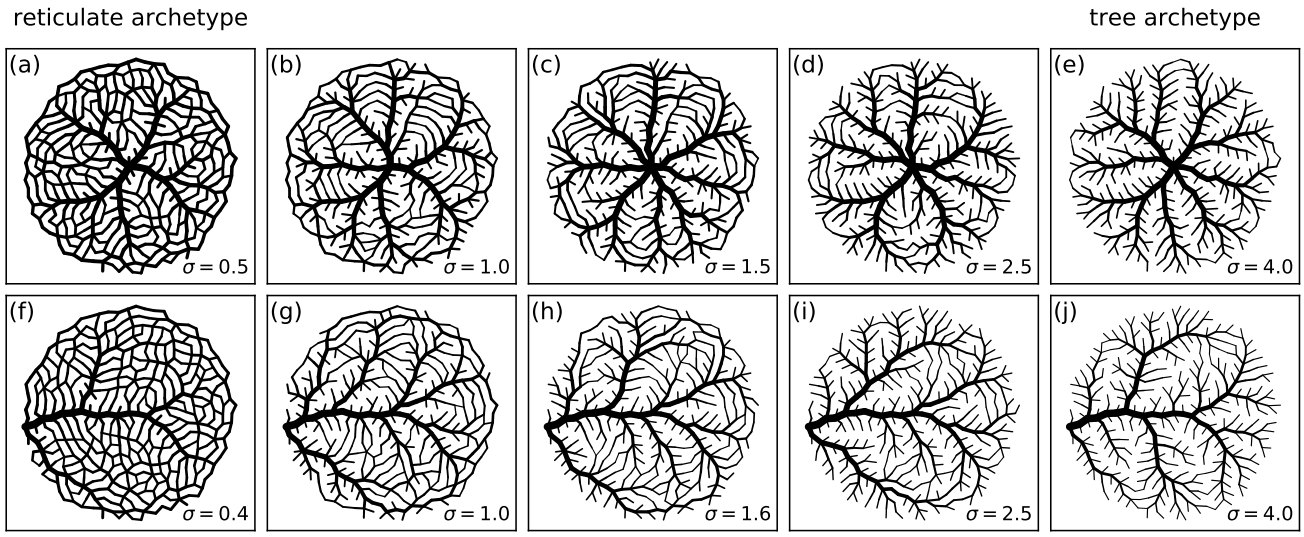


FIG. S6. The equivalent of Fig. 2 from the main paper for exponential sources. Networks on the Pareto front behave qualitatively analogously to Gaussian sources.

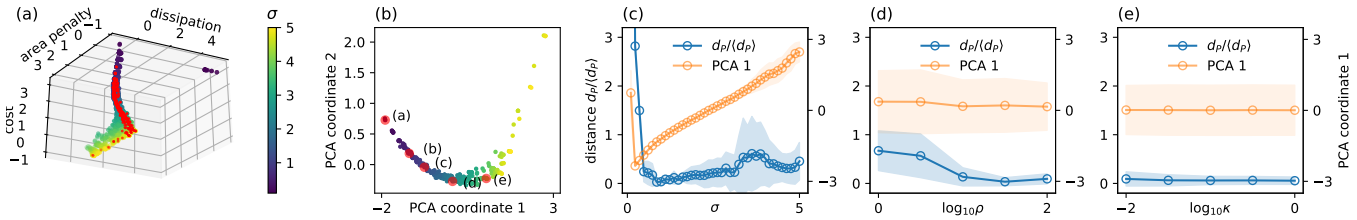


FIG. S7. Equivalent of Fig. 3 from the main paper for the case of exponential sources with an inlet at the center of the network. Results are qualitatively similar to those from the main paper. The marked networks in panel (b) correspond to the networks (a–e) from Fig. S6.

Random sources

In this subsection we show results from random fluctuations. We consider fluctuating states

$$S_j^{(i)} = \begin{cases} -k & \text{with probability } p \\ 0 & \text{with probability } 1-p \end{cases} \tag{S15}$$

for $j = 1, \ldots, N-1$. The source is normalized to $(S_i)_0 = \sum_{j>0}(S_i)_j = 1$. This normalization sets the value of of the constant k. In the case of these random fluctuations, we consider fluctuation averages over 100 different arrangements

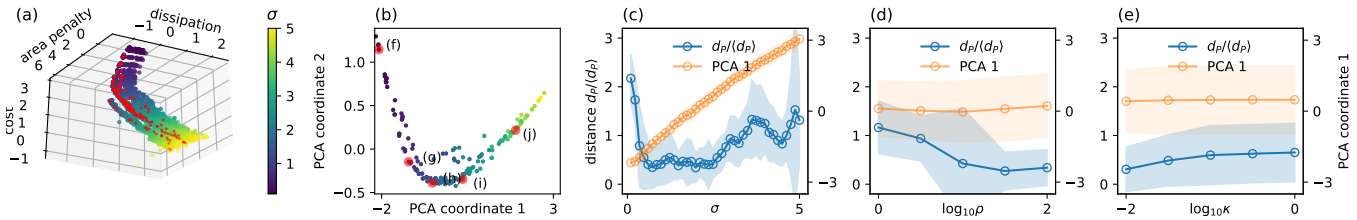


FIG. S8. Equivalent of Fig. 3 from the main paper for the case of exponential sources with an inlet at the boundary the network. Results are qualitatively similar to those from the main paper. The marked networks in panel (b) correspond to the networks (f–j) from Fig. S6.

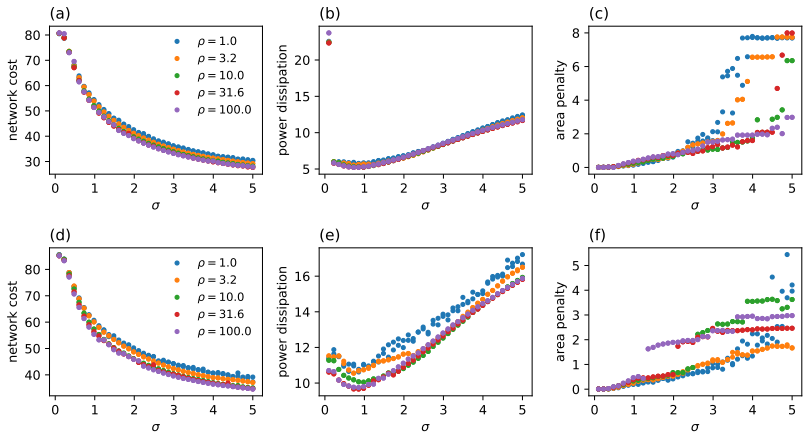


FIG. S9. Network measures for exponential sources at fixed $\kappa = 1.0$. (a–c) A single inlet at the center of the network. (d–f) A single inlet at the left side of the network.

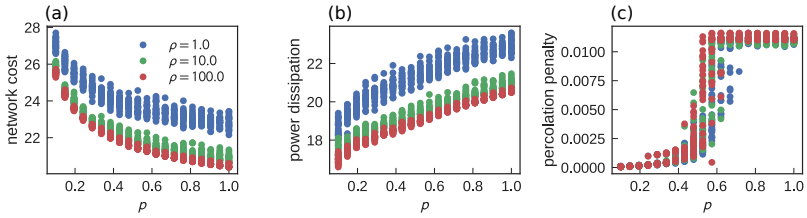


FIG. S10. Dependence of network phenotypes on probability for randomly distributed fluctuations with one source at the left boundary for fixed $\kappa = 1.0$. Two distinct phases can be discerned in the percolation penalty with a sharp transition between them. For $p > 0.5$, no more loops are produced in the networks such that the percolation penalty remains at a large value. For $p < 0.5$, the networks are well-connected.

of the sources that all satisfy the above probabilistic condition. For these types of fluctuations, the resulting network often does not connect each node in the original lattice to the source node. Thus, our metrics such as the percolation penalty, network cost, and uniform energy cannot be directly compared anymore. Yet, inspecting the simulation results for various values of p shows that this model does not reproduce strongly hierarchically ordered networks, see Fig. S11 for the case of leaf-like boundary conditions as an example.

Comparing also with Fig. S10, we observe a sharprhos transition between a well-connected network for $p < 0.5$ and a minimally connected topological tree for $p > 0.5$. The case $p = 0.5$ was considered in detail in Ref. [34].

In all cases, we scanned a parameter range of 5 logarithmically distributed points between $\rho = 1$ and $\rho = 100$, 5 logarithmically distributed points between $\kappa = 0.01$ and $\kappa = 1$, and 40 linearly distributed points between $p = 0.1$ end $p = 1$. For each combination, we took 2 samples with random initial conditions.

Uniform + moving point sources

Here we consider a source term that is composed of a contribution from uniform sinks on the network, and one from random sinks. Specifically, we consider

$$S_j^{(i)} = \delta_{j0} - \alpha\,(1 - \delta_{j0})(1 - e + e\,\delta_{ij}). \tag{S16}$$

The parameter e controls the relative importance of both terms, and the normalization factor α is chosen to enforce $\sum_j S_j^{(i)} = 0$. If $e = 0$, there are uniform sinks and we expect a hierarchical tree network. If $e = 1$, the sinks are fully random, and we expect a fully reticulate network analogous to the $\sigma \to 0$ case for a distance-dependent fluctuation function. Numerically, we observe that networks remain trees until approximately $e \approx 0.96$. Hence, we explore the parameter range $0.96 \leq e \leq 1.0$ in detail.

Fig. S12 corresponds to Fig. 2 from the main paper, and Figs. S13 and S14 correspond to Fig. 3 from the main paper for inlets at the center or at the left. Again we find qualitatively similar results to the case investigated in the

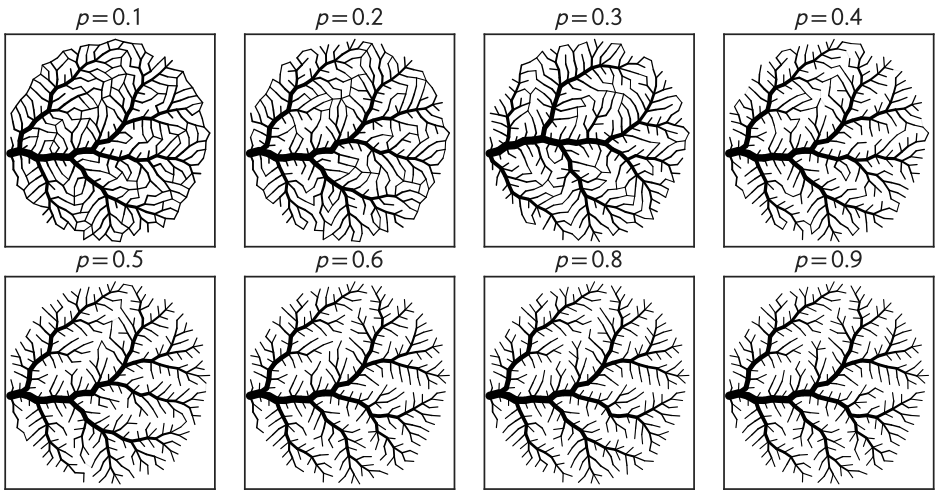


FIG. S11. Random networks for a source at the left boundary and various probabilities p of any node being a source. For $p > 0.5$, the networks are trees. We used parameter values $\kappa = 1, \rho = 99$.

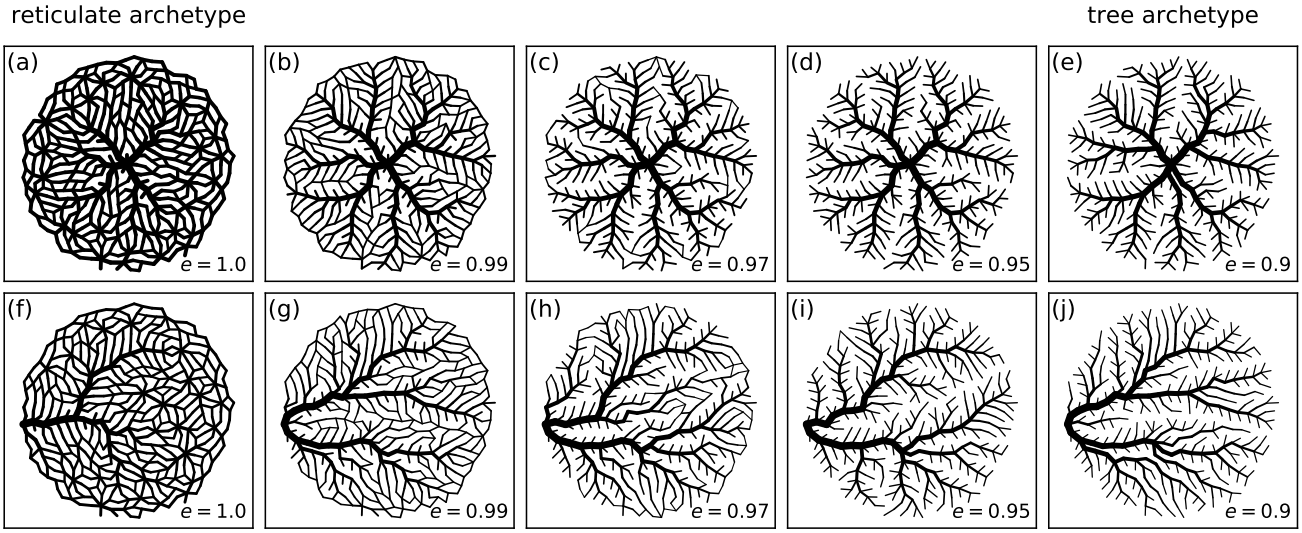


FIG. S12. The equivalent of Fig. 2 from the main paper for the uniform sources + moving sink model. Networks on the Pareto front behave qualitatively analogously to Gaussian sources, as discussed in the main paper, and the parameter e controls reticulation.

main paper when it comes to the ability of the parameter e to interpolate along the Pareto front. However, the Pareto front is more fragmented and shows distinct clusters as opposed to the clear approximately 1-dimensional geometry found for Gaussian or exponential sources.

In all cases, we scanned a parameter range of 5 logarithmically distributed points between $\rho = 1$ and $\rho = 100$, 5 logarithmically distributed points between $\kappa = 0.01$ and $\kappa = 1$, and 20 logarithmically distributed points between $e = 0.9$ end $e = 1$. For each combination, we took 2 samples with random initial conditions.

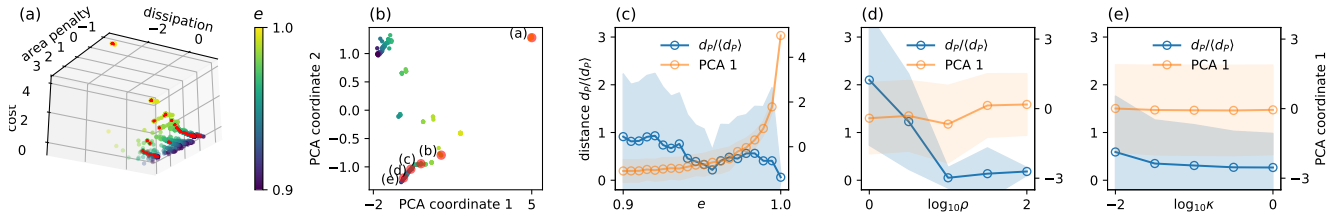


FIG. S13. Equivalent of Fig. 3 from the main paper for the case of uniform + moving point sources with an inlet at the center of the network. Results are qualitatively similar to those from the main paper in terms of parametrizing the Pareto front, but the shape of the Pareto front shows distinct clusters, and is not 1-dimensional. The marked networks in panel (b) correspond to the networks (a–e) from Fig. S12.

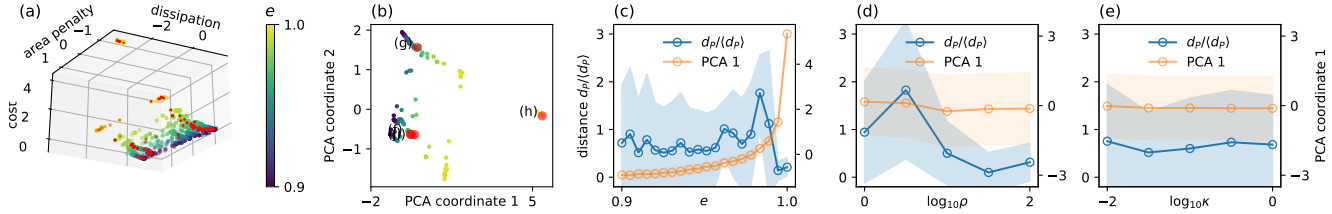


FIG. S14. Equivalent of Fig. 3 from the main paper for the case of uniform + moving point sources with an inlet at the left of the network. Results are qualitatively similar to those from the main paper in terms of parametrizing the Pareto front, but the shape of the Pareto front shows distinct clusters, and is not 1-dimensional. The marked networks in panel (b) correspond to the networks (f–j) from Fig. S12.

Fluctuation average and eigendecomposition of the source covariances

As shown the the preceding section, the vector of flows can be written as a linear map acting on the vector of sources,

$$\mathbf{F} = KL^{-1}\Delta\left(\Delta^\top KL^{-1}\Delta\right)^\dagger \mathbf{S} \tag{S17}$$

$$= A\,\mathbf{S}. \tag{S18}$$

The fluctuation average over several sources can therefore be expressed as

$$\langle F_e^2\rangle = \frac{1}{N}\sum_i (\mathbf{e}^\top A\mathbf{S}^{(i)})^2 \tag{S19}$$

$$= \mathbf{e}^\top A \underbrace{\frac{1}{N}\left(\sum_i \mathbf{S}^{(i)}(\mathbf{S}^{(i)})^\top\right)}_{=C} A^\top \mathbf{e}, \tag{S20}$$

where $\mathbf{e}$ is the unit vector corresponding to edge e. The matrix C is precisely the matrix of (uncentered) covariances between the source states. Using the eigendecomposition $C = \sum_j \rho_j \mathbf{r}_j \mathbf{r}_j^\top$, we find

$$\langle F_e^2\rangle = \mathbf{e}^\top A \sum_j \rho_j \mathbf{r}_j \mathbf{r}_j^\top A^\top \mathbf{e} \tag{S21}$$

$$= \sum_j \rho_j (\mathbf{e}^\top A\mathbf{r}_j)^2, \tag{S22}$$

which corresponds to Eq. (5) in the main paper with $R_e^{(j)} = \mathbf{e}^\top A\mathbf{r}_j$.

The eigenvalues of the correlation matrix C generally decay rapidly for large correlation lengths σ, as shown in Fig. S15.

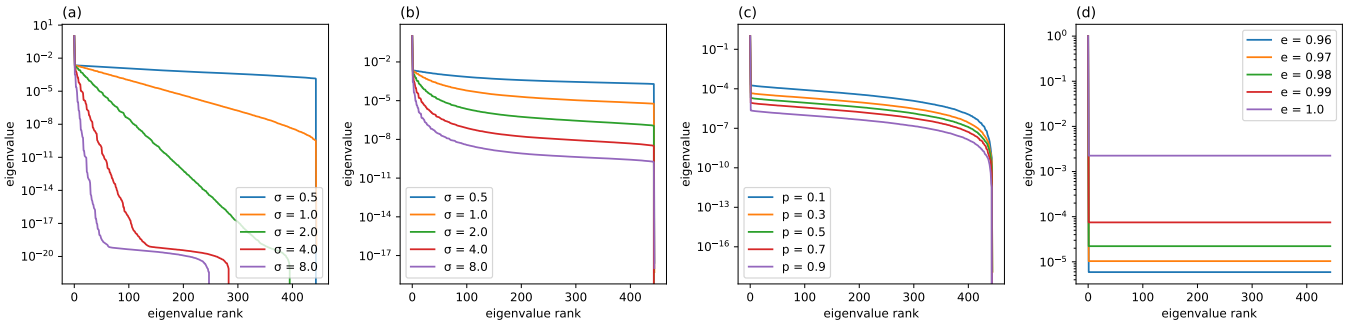


FIG. S15. The eigenvalues of the correlation matrix C for the network topology considered here and in the main paper, with an inlet at the center of the network. (a) Gaussian sources (b) exponential sources (c) random sources (d) uniform + moving point sources. All correlation matrices are characterized by a single, dominant eigenvalue whose eigenvector approximately corresponds to a single inlet uniform with uniform sinks. When the parameters are chosen such that the other eigenvalues are small, only this dominant eigenvalue is relevant, and leads to a hierarchical tree network topology.

Covariance matrix for uncorrelated fluctuations

As long as the fluctuation function satisfies $f(0) = 1$ and $f(\infty) = 0$, the limit $\sigma \to 0$ will lead to uncorrelated fluctuations in the statistical sense. The sources become

$$S_j^{(i)} = \delta_{j0} + (1 - \delta_{j0})\delta_{ji},$$

which corresponds to a single sink randomly placed at node i. We now proceed to calculate the covariance matrix between different node sinks.

Statistically, each of the N sink nodes is active with probability $1/N$ and strength 1. Thus,

$$\langle S_j \rangle = \frac{1}{N} \tag{S23}$$

for $j > 0$. We can further calculate

$$\langle S_i S_j \rangle = \frac{1}{N}\frac{1}{N} \tag{S24}$$

for $i \neq j$ and $i, j > 0$ because the sources are independent. Because $\langle S_i^2 \rangle = \frac{1}{N}$, we find the general expression

$$\langle S_i S_j \rangle = \frac{1}{N^2} + \left(\frac{1}{N} - \frac{1}{N^2}\right)\delta_{ij}, \tag{S25}$$

such that finally, the statistical covariance matrix becomes

$$\langle S_i S_j \rangle - \langle S_i \rangle \langle S_j \rangle = \left(\frac{1}{N} - \frac{1}{N^2}\right)\delta_{ij}, \tag{S26}$$

which is proportional to the unit matrix and therefore corresponds to uncorrelated fluctuations.